Smooth Lagrangian Crack Band Model Based on Spress-Sprain Relation and Lagrange Multiplier Constraint of Displacement Gradient

Anh Tay Nguyen
Department of Mechanical Engineering,
Northwestern University,
2145 Sheridan Road,
Evanston, IL 60208
e-mail: anhnguyen2025@u.northwestern.edu

Houlin Xu
Department of Civil and Environmental
Engineering,
Northwestern University,
2145 Sheridan Road,
Evanston, IL 60208
e-mail: houlinxu2020@u.northwestern.edu

Karel Matouš
Professor
Aerospace and Mechanical Engineering,
University of Notre Dame,
Notre Dame, IN 46556
e-mail: kmatous@nd.edu

Zdeněk P. Bažant[1]
McCormick Institute Professor and W. P. Murphy
Professor of Civil and Mechanical Engineering and
Materials Science,
Northwestern University,
2145 Sheridan Road, CEE/A135,
Evanston, IL 60208
e-mail: z-bazant@northwestern.edu

A preceding 2023 study argued that the resistance of a heterogeneous material to the curvature of the displacement field is the most physically realistic localization limiter for softening damage. The curvature was characterized by the second gradient of the displacement vector field, which includes the material rotation gradient, and was named the "sprain" tensor, while the term "spress" is here proposed as the force variable work-conjugate to "sprain." The partial derivatives of the associated sprain energy density yielded in the preceeding study, sets of curvature resisting self-equilibrated nodal sprain forces. However, the fact that the sprain forces had to be applied on the adjacent nodes of a finite element greatly complicated the programming and extended the simulation time in a commercial code such as ABAQUS by almost two orders of magnitude. In the present model, Smooth Lagrangian Crack Band Model (slCBM), these computational obstacles are here overcome by using finite elements with linear shape functions for both the displacement vector and for an approximate displacement gradient tensor. A crucial feature is that the nodal values of the approximate gradient tensor are shared by adjacent finite elements. The actual displacement gradient tensor calculated from the nodal displacement vectors is constrained to the approximate displacement gradient tensor by means of a Lagrange multiplier tensor, either one for each element or one for each node. The gradient tensor of the approximate gradient tensor then represents the approximate third-order displacement curvature tensor, or Hessian of the displacement field. Importantly, the Lagrange multiplier behaves as an externally applied generalized moment density that, similar to gravity, does not affect the total strain-plus-sprain energy density of material. The Helmholtz free energy of the finite element and its associated stiffness matrix are formulated and implemented in a user's element of ABAQUS. The conditions of stationary values of the total free energy of the structure with respect to the nodal degrees-of-freedom yield the set of equilibrium equations of the structure for each loading step. One- and two-dimensional examples of crack growth in fracture specimens are given. It is demonstrated that the simulation results of the three-point bend test are independent of the orientation of a regular square mesh, capture the width variation of the crack band, the damage strain profile across the band, and converge as the finite element mesh is refined. [DOI: 10.1115/1.4063896]

Keywords: fracture mechanics, continuum mechanics, damage mechanics, sprain energy, spress-sprain relations, quasi-brittle materials, material heterogeneity, nonlocal continuum, gradient models, numerical simulation, finite element method, localization limiters, computational mechanics, failure criteria, constitutive modeling of materials

1 Introduction

In 1962, Clough [1–3] pioneered finite element analysis (FEA) of continuum bodies. Using his variationally derived constant-strain finite element (FE) of an elastic continuum [3], he launched computational fracture mechanics by his finite element solution of the overall stress state in the cracked Norfolk Dam (Fig. 1), which mesmerized the structural engineering community of that time. Yet, after the lapse of 61 years, no completely satisfactory computational model for fracture exists today. A model in the preceding 2023 paper [4], which introduced the concept of *sprain*, came close except for severe programming and computational obstacles due to the fact that sprain forces had to be applied on the nodes adjacent to a finite element. In this paper, an improved
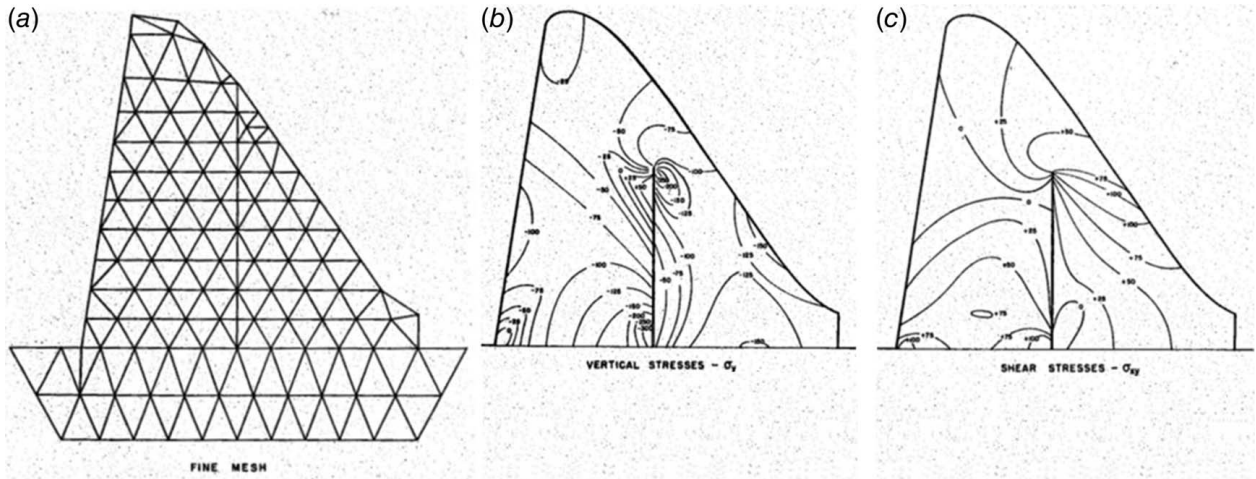
Fig. 1   Clough's 1962 elastic finite element solution of the overall stress state in the cracked Norfolk Dam [1]: (a) mesh discretization of the dam, (b) vertical stresses σ_y contour, and (c) shear stresses σ_{xy} contour of the dam

model, namely Smooth Lagrangian Crack Band Model (slCBM) overcomes these challenges by introducing the new concept of spress as a force variable work-conjugate to the sprain, and by constraining the actual displacement gradient calculated from the nodal displacement vectors to the approximate gradient through the use of Lagrange multipliers. By doing so, finite elements with linear shape functions for both the displacement vector and for the approximate displacement gradient tensor can be used, thus avoiding the need of applying sprain forces on adjacent nodes.

By extensive comparisons with numerous experiments, a recent study in 2022 [5] demonstrated deficiencies of the recently popular computational fracture models, particularly the peridynamics and phase field. Relying on 11 different distinctive classical fracture experiments, including the results of the recently developed gap test [6–8], that study [5] identified serious inherent limitations of peridynamics and of all line crack models including the linear elastic fracture mechanics (LEFM), cohesive crack model, extended finite element method (XFEM), and phase-field model. It further highlighted the misleading nature of model "verifications" by "non-distinctive" tests, i.e., tests that can be fitted closely by very different models [9], commonly abused in many computational papers.

The adoption of displacement vector curvature (or Hessian) [4] as a localization limiter was inspired by the recent discovery of the gap test [6,7] and by comparisons of the classical 1983 crack band model (CBM) with material characteristic length [10–12] to the phase-field models and peridynamics [5,9]. The present theory can also be regarded as a generalization of the classical strain-gradient models [13–21], which differ mainly by missing the material rotation gradient that is important for shear fracture. These theories were developed in the works of Bažant and Jirásek and Gao et al. [13,22], and culminated in the very effective mechanism-based strain-gradient theory of Huang et al. [23], whose objective was hardening plasticity and the effect of geometrically necessary dislocations, rather than damage and fracture. A strain-gradient theory for damage in concrete was formulated by Cusatis et al. [14,15]. For comparisons with experiments and for applications in structural design, it is essential to use a realistic damage constitutive relation, for which the microplane models are essential [24–27]. Achieving superior comparisons with distinctive tests of concrete in Ref. [5] was enabled by the use of not only crack band model [10–12] but also the microplane model M7. The present use of displacement vector curvature also implies significant changes for continuum mechanics of damage in heterogeneous materials, including the homogenization theories [22,23,28–35].

A more detailed review of the subject, including the history, was presented in 2023 in the same journal [4], along with a broader historical review from the same perspective as here. Therefore, it would be superfluous to duplicate it.

2   Spress-Sprain Continuum

As in the preceding study, the total Helmholtz free energy density, $\bar{\Psi}(\boldsymbol{\varepsilon}, \boldsymbol{\xi})$, is defined as the sum of the classical strain energy, $\Psi(\boldsymbol{\varepsilon})$, and the sprain energy $\Phi(\boldsymbol{\xi})$—a new concept;

$$\bar{\Psi}(\boldsymbol{\varepsilon}, \boldsymbol{\xi}) = \Psi(\boldsymbol{\varepsilon}) + \Phi(\boldsymbol{\xi}) \tag{1}$$

where $\boldsymbol{\varepsilon}$ is the (linearized) strain tensor with Cartesian components $\varepsilon_{ij} = \frac{1}{2}(u_{i,j} + u_{j,i})$, u_i being the displacements in Cartesian coordinates x_i ($i = 1, 2, 3$ in 3D or $1, 2$ in 2D), and $\boldsymbol{\xi}$ is the sprain tensor, a third-order tensor of components

$$\xi_{ijk} = l_0 u_{i,jk}, \quad \eta_{ijk} = \varepsilon_{ij,k}, \quad u_{i,jk} = \eta_{ijk} + \omega_{ij,k} \tag{2}$$

Here η_{ijk} is the classical strain-gradient tensor, used in many strain-gradient theories of plasticity and damage (e.g., Refs. [23,36–38]), and $\omega_{ij,k} = \frac{1}{2}(u_{i,j} - u_{j,i})$ is the gradient of the (linearized) material rotation tensor, which all have the dimension of m^{-1}. The tensor ξ_{ijk} was introduced in Ref. [4] as a dimensionless definition of sprain (note that it was denoted as η_{ijk} but this is now changed because it conflicted with the long established notation for the strain gradient). Tensor $\omega_{ij,k}$ was introduced in the preceding work [4] as an essential feature of the sprain theory, which is missing from the classical strain-gradient theories.

For small deformations, the classical definition of stress, σ_{ij}, and the presently proposed definition of *spress* are

$$\sigma_{ij} = \frac{\partial \Psi(\boldsymbol{\varepsilon})}{\partial \varepsilon_{ij}}, \quad s_{ijk} = \frac{\partial \Phi(\boldsymbol{\xi})}{\partial \xi_{ijk}} = \frac{1}{l_0} \frac{\partial \Phi(\boldsymbol{\xi})}{\partial u_{i,jk}} \tag{3}$$

Here and in Eq. (2), the material characteristic length, l_0 (which is what characterizes the size of the fracture process zone (FPZ) size and indirectly limits damage localization, through $\boldsymbol{\xi}$), is introduced to make the dimensions or σ_{ij} and s_{ijk} the same, i.e., N/m^2, and to conform to Φ having the dimension of J/m^3 or N/m^2. In the previous work, the term *sprain* was borrowed from orthopedic medicine where it means damage of a ligament that is spread over a finite length while causing no rupture, and the term *spress* is introduced here as the third-order variable work-conjugate to sprain (and analogous to stress).

The computations in the previous study [4] used, instead of s_{ijk}, the sprain force $f_n = b A_n \partial \Phi/\partial \boldsymbol{u}$, which is the derivative of the sprain energy with respect to the nodal displacement vector $\boldsymbol{u}$ multiplied by the tributary material volume $b A_n$ of node n in a regular finite element mesh (b = body thickness, A_n = tributary area). However, this approach required applying self-equilibrated forces on nodes adjacent to a given finite element, which turned out to be very cumbersome for programming, especially in commercial

programs such as ABAQUS, and extended the running time by almost two orders of magnitude. For computations, it is advantageous to introduce a second-order tensor field, $\boldsymbol{\zeta}$, of components ζ_{ij}, to serve as an approximation of displacement gradient field $u_{i,j}$ (dimensionless). Considering the fields of u_i and ζ_{ij} as independent, each of them may be now represented by C_0 finite elements with linear shape functions, which will greatly simplify FE analysis. To introduce the idea, let us first give a simple example.

3 Inspiration From One-Dimensional Gradient Constraint

Simple 1D Example: For a one-dimensional (1D) line element of length h along the axial coordinate x, with nodal displacements u_r and u_{r+1} at nodes r and $r+1$, the displacement gradient approximation is obviously given by

$$\frac{u_{r+1} - u_r}{h} \approx \frac{\zeta_r + \zeta_{r+1}}{2} \qquad (4)$$

where ζ_r and ζ_{r+1} are the nodal approximate displacement gradients at nodes r and $r+1$, respectively. The sprain (or the curvature of the displacement field in axial coordinate $x_1 = x$) can then be simply approximated without any need for adjacent nodes $r-1$ or $r+2$. Indeed,

$$u_{x,xx} \approx \frac{\zeta_{r+1} - \zeta_r}{h} \qquad (5)$$

Generalizations: It will be seen that, for general situations, the actual displacement gradient tensor $\nabla \boldsymbol{u}$ and the approximate displacement gradient tensor $\boldsymbol{\zeta}$ are best matched by imposing an approximate constraint through a Lagrange multiplier. To this end, we first note that this approximate constraint, Eq. (4), can be more generally obtained from the condition

$$\int_V (\nabla \boldsymbol{u} - \boldsymbol{\zeta}) \, dV = 0 \quad \text{or} \quad \frac{\partial}{\partial \lambda} \int_V \lambda (\nabla \boldsymbol{u} - \boldsymbol{\zeta}) \, dV = 0 \qquad (6)$$

over volume V of a finite element. Parameter λ is inserted in anticipation of a variational approach in which the derivative $\partial/\partial \lambda$ plays the role of a minimizing condition of the integral.

Substituting the 1D linear shape (or interpolation) functions shown in Fig. 2(b) for each of u and ζ, and integrating over
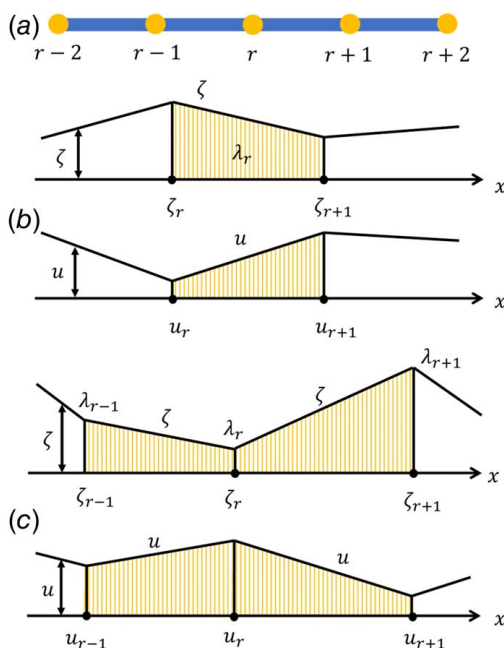

Fig. 2 (a) A row of one-dimensional finite elements with (b) linear shape functions for both displacement u and its gradient $u_{,x}$, and (c) approximate matching of $u_{,x}$ with ζ

length coordinate x within finite element $(r, r+1)$ of length h, we verify that our approximate constraint may be stated as

$$\frac{\partial}{\partial \lambda} \int_{x_r}^{x_{r+1}} \lambda (\nabla u - \zeta) \, dx = \frac{u_{r+1} - u_r}{h} - \frac{\zeta_r + \zeta_{r+1}}{2} = 0 \qquad (7)$$

which is equivalent to the approximation in Eq. (4).

4 Finite Element With Approximate Displacement Gradient Constrained by Lagrange Multiplier

In 1D analysis, the match is exact for Eq. (6), but in 2D or 3D analysis, we must look for the optimum match. Therefore, inspired by Eq. (7), we now combine the constraint in Eq. (6) having the form of an extremum stationarity condition, with the minimizing (or stationarity) condition of the potential energy, Π, of the structure. For the constrained optimization, the foregoing considerations suggest adopting the method of undetermined Lagrange multiplier λ [39, p. 442] (previously used in FE for other purposes, e.g., Refs. [40–42]). To use the simple C_0 finite elements in two (or three) dimensions (2D or 3D), we introduce, like for 1D, a separate dimensionless second-order tensor field, $\boldsymbol{\zeta}$, of components ζ_{ij}, which is equal to the first gradient of the displacement field

$$\boldsymbol{\zeta} = \nabla \boldsymbol{u} \qquad (8)$$

and the sprain tensor $\boldsymbol{\xi}$ is then represented through the first gradient of $\boldsymbol{\zeta}$ multiplied by the characteristic length l_0

$$\boldsymbol{\xi} = l_0 \nabla \boldsymbol{\zeta} \qquad (9)$$

Now we may introduce the following continuous formulation of the extended potential energy of the whole structural system, which represents the internal energy, W_{in}, minus the external energy, W_{ex} (equivalent to the work of given applied loads),

$$\Pi(\boldsymbol{u}, \boldsymbol{\zeta}, \lambda) = W_{in} - W_{ex} \quad \text{where} \qquad (10)$$

$$W_{in} = \int_V \boldsymbol{\Psi}[\boldsymbol{\varepsilon}(\boldsymbol{u})] \, dV + \int_V \boldsymbol{\Phi}[\boldsymbol{\xi}(\boldsymbol{\zeta})] \, dV - \int_V \lambda (\nabla \boldsymbol{u} - \boldsymbol{\zeta}) \, dV \qquad (11)$$

$$W_{ex} = \int_V \boldsymbol{f}(\boldsymbol{x}) \cdot \boldsymbol{u} \, dV \qquad (12)$$

Here V is the structure volume (which is equivalent to the area multiplied by a unit thickness for 2D analysis), $\boldsymbol{f}(\boldsymbol{x})$ is the given distributed applied load vector acting on displacement vector $\boldsymbol{u}$ but is independent of it. Since $\boldsymbol{\xi}$ is a function of $\boldsymbol{\zeta}$ (Eq. (9)), the sprain energy density $\boldsymbol{\Phi}$ is now a function of $\boldsymbol{\zeta}$. To couple the strain energy and the sprain energy, Eq. (8) is added to the internal energy expression as the constraint condition in a weak sense, through the use of the Lagrange multiplier λ, which is a variable throughout the structure.

Physical Motivation: Looking from a mechanics point of view, one could often find a physical motivation for the Lagrange multipliers [41,42]. Note the similarity of the last integral in Eq. (11) and right-hand side of Eq. (12). In the latter, $\boldsymbol{f}(\boldsymbol{x}) \cdot \boldsymbol{u}$ represents the external work done on displacement $\boldsymbol{u}$ by a constant gravity force $\boldsymbol{f}$ (independent of $\boldsymbol{u}$) per unit volume. So, in the former, λ (dimension Pa) can be seen as a generalized moment per unit volume doing external work on the gradient difference, like some constant pseudo-gravity (independent of the gradient difference). This external work may be likened to the applied force term in the potential energy, i.e., $-\int_V \boldsymbol{f}(\boldsymbol{x}) \cdot \boldsymbol{u} \, dV$. For $\boldsymbol{u}$, the minimizing condition is $\partial W/\partial u = 0$. By analogy of pseudo-gravity, this explains physically the last extremum condition $\partial W/\partial \lambda = 0$. The fact that the work of λ is external, not part of the internal energy density, is important. This work is only added to the definition of the internal energy expression in Eq. (11) as a constraint condition in a weak sense to couple the strain energy and the sprain energy as explained earlier.

Why not a quadratic penalty? Indeed, one could impose it instead of using Lagrange multiplier. However, a penalty (with stiffness K_p)

would have to consist of a quadratic form $K_p(\nabla u - \zeta)^2/2$, which would have the physical meaning of adding fictitious additional strain energy to the system. If the quadratic penalty is not minimized exactly to zero, one would end up with a system containing some non-existent excessive strain energy. The "beauty" of the Lagrange multiplier method is that it represents a fictitious externally applied moment density (or pseudo-gravity) and adds nothing to the internal energy content of the structure.

Remark 1. Another way to implement the sprain theory in FE programs could be to ensure the field of displacement u_i to have at least C_1 continuity, which would also avoid the cumbersome need for applying curvature resisting forces on the nodes of adjacent elements. It might seem that the quadratic or cubic elements, which are usually called the C_1 and C_2 continuity elements would be suitable for this approach. However, they actually provide the C_1 continuity only along the element boundaries, while the continuity of displacement gradients $u_{i,j}$ in directions normal to the element boundaries is not satisfied, which is essential in this problem. The C_1 continuity normal to element boundary could be satisfied only with quartic elements using the same fourth degree shape functions as those for thin plate bending [40]. This approach, too, would avoid applying sprain forces to the adjacent nodes since the resistance to sprain would be embedded within the element stiffness matrix. However, it would be computationally inefficient compared to the present approach and also would be "too smooth" for fracture modeling. ∎

5 Spress-Sprain Relation of the Material

The spress-sprain relation is based on the sprain energy density whose only purpose is to resist the curvature of the displacement field. This relation is a material property but it is not a constitutive relation in the standard sense because it deals with the second gradient of displacement. This was done in a rather hypothetical way in the preceding study [4], in which it was assumed that what is here named the *spress* is controlled through a constant threshold C, after which each component of the spress tensor grows from zero with a sprain stiffness κ that decreases with the inelastic volumetric strain ε_V. Better understanding of the spress-sprain relation will necessitate discrete particle simulation of sprain.

It is proposed here that only spresses and sprains of the same subscript ijk interact (i.e., they are not cross-related). Some possible forms, which are still being studied in the context of Lagrange multiplier constraint, are given in tensorially consistent form as follows:

$$s_{ijk} = \kappa \langle |\boldsymbol{\xi}| - C \rangle \frac{\xi_{ijk}}{|\boldsymbol{\xi}|} \tag{13}$$

$$\text{or} \quad s_{ijk} = \kappa \left(\frac{|\boldsymbol{\xi}|}{C} \right)^n \frac{\xi_{ijk}}{|\boldsymbol{\xi}|} \tag{14}$$

in which

$$C = C_0 + C_1 \varepsilon_V'' \tag{15}$$

where C is the sprain threshold, κ is the sprain stiffness, ε_V'' is the inelastic part of the total volumetric strain ε_V, while C_0, C_1, and n are empirical fitting parameters.

The threshold C and the sprain stiffness κ are here considered as constants, although it is suspected that the sprain stiffness κ should be considered as a function of either the total volumetric strain, ε_V or of its inelastic part ε_V'' (as in Ref. [4]), or $|\boldsymbol{\xi}|$. The expression for s_{ijk} in Eq. (14) is smooth, which might help the convergence of the iterative scheme. A high exponent such as $n = 10$ may have to be used so that the sprain would have a negligible effect in the elastic regime.

After further modeling experience, which showed that decreasing the sprain stiffness κ requires further investigation (and that a sharp nonzero threshold C might be unnecessary and might even slow the convergence rate), we consider the relation shown in Eq. (13) with $C = 0$ and a constant κ, i.e., $s_{ijk} = \kappa \xi_{ijk}$. Taking $C = 0$ might be a reasonable simplification because, as argued here, the displacement curvatures in the elastic range are negligible and the sprain

energy is not big enough to have a substantial influence on the strain energy and to change the elastic behavior of the structure. However, this may not hold if the structure contains defects that cause stress concentration.

6 Variational Formulation

The strain energy and the sprain energy density are rewritten in indices notation using the material relation between $\boldsymbol{\sigma}(\boldsymbol{\varepsilon})$ and the spress-sprain relation $s(\boldsymbol{\xi})$ as follows:

$$\Psi = \int_{\boldsymbol{\varepsilon}} \sigma(\boldsymbol{\varepsilon})_{ij} \, d\varepsilon_{ij}, \quad \Phi = \int_{\boldsymbol{\xi}} s(\boldsymbol{\xi})_{ijk} \, d\xi_{ijk} \tag{16}$$

Using Eq. (16), Eq. (10) becomes

$$\Pi(u_i, \zeta_{ij}, \lambda_{ij}) = \int_V \left\{ \int_{\boldsymbol{\varepsilon}} \sigma_{ij} \, d\varepsilon_{ij} + \int_{\boldsymbol{\xi}} s_{ijk} \, d\xi_{ijk} - f_i \cdot u_i - \lambda_{ij} \cdot (u_{i,j} - \zeta_{ij}) \right\} dV \tag{17}$$

where $i, j = 1, 2, 3$. The variational conditions of the minimum of the potential energy and of the constraint extremum then are

$$\frac{\partial \Pi(u_i, \zeta_{ij}, \lambda_{ij})}{\partial u_i} \delta u_i = \int_A \left\{ \sigma_{ij} \, \delta \varepsilon_{ij} - f_i \, \delta u_i - \lambda_{ij} \, \delta u_{i,j} \right\} dV$$

$$= \int_V \left\{ -\sigma_{ij,j} - f_i + \lambda_{ij,j} \right\} \delta u_i \, dV + [\cdots]_V = 0 \tag{18}$$

$$\frac{\partial \Pi(u_i, \zeta_{ij}, \lambda_{ij})}{\partial \zeta_{ij}} \delta \zeta_{ij} = \int_V \left\{ s_{ijk} \, \delta \xi_{ijk} + \lambda_{ij} \, \delta \zeta_{ij} \right\} dV$$

$$= \int_V \left\{ -l_0 s_{ijk,k} + \lambda_{ij} \right\} \delta \zeta_{ij} \, dV + [\cdots]_V = 0 \tag{19}$$

$$\frac{\partial \Pi(u_i, \zeta_{ij}, \lambda_{ij})}{\partial \lambda_{ij}} \delta \lambda_{ij} = \int_V - \left\{ u_{i,j} - \zeta_{ij} \right\} \delta \lambda_{ij} \, dV = 0 \tag{20}$$

Since Eqs. (18)–(20) must also hold for each subpart of the body, we must require that locally

$$\sigma_{ij,j} + f_i - \lambda_{ij,j} = 0 \tag{21}$$

$$l_0 s_{ijk,k} - \lambda_{ij} = 0 \tag{22}$$

$$u_{i,j} - \zeta_{ij} = 0 \tag{23}$$

7 Finite Element Discretization With Sprain Variables

7.1 1D Formulation. We first present the spatial discretization by finite element for one-dimensional analysis. For an one-dimensional finite element which has two nodes of coordinate x_1 and x_2, respectively, and a constant cross-sectional area A, the displacement field $\boldsymbol{u}$ and the zeta field $\boldsymbol{\zeta}$ in each element are approximated by a linear function interpolated from the corresponding nodal values at two nodes of the element, while λ will be a constant across the element.

$$\boldsymbol{u} = \boldsymbol{N}(x)\tilde{\boldsymbol{u}} \quad \text{where} \quad \tilde{\boldsymbol{u}}^T = [u_1, u_2] \tag{24}$$

$$\boldsymbol{\zeta} = \boldsymbol{N}(x)\tilde{\boldsymbol{\zeta}} \quad \text{where} \quad \tilde{\boldsymbol{\zeta}}^T = [\zeta_1, \zeta_2] \tag{25}$$

For one-dimensional analysis, strain $\varepsilon_x = du/dx = d(\boldsymbol{N}(x)\tilde{\boldsymbol{u}})/dx = \boldsymbol{N}_{,x}(x)\tilde{\boldsymbol{u}}$ and sprain $\xi_x = d\zeta/dx = d(\boldsymbol{N}(x)\tilde{\boldsymbol{\zeta}})/dx = \boldsymbol{N}_{,x}(x)\tilde{\boldsymbol{\zeta}}$. In addition, $\nabla \boldsymbol{u} = d\boldsymbol{u}/dx = \boldsymbol{N}_{,x}(x)\tilde{\boldsymbol{u}}$. In order to minimize the total potential energy Π, we set the partial derivative of the total potential energy with respect to the degrees-of-freedom (DOF) to be zero

$$\boldsymbol{f}_{int}^u = \frac{\partial \Pi}{\partial \tilde{\boldsymbol{u}}^T} = A \left\{ \int_{x_2}^{x_1} \boldsymbol{N}^T_{,x}(x) \sigma_x \, dx - \lambda \int_{x_2}^{x_1} \boldsymbol{N}^T_{,x}(x) \, dx - \int_{x_2}^{x_1} \boldsymbol{N}^T(x) f(x) \, dx \right\} \tag{26}$$

$$f_{int}^{\zeta} = \frac{\partial \Pi}{\partial \tilde{\zeta}^T} = A \left\{ \int_{x_2}^{x_1} N^T,_x(x) s_x \, dx + \lambda \int_{x_2}^{x_1} N^T(x) \, dx \right\} \qquad (27)$$

$$f_{int}^{\lambda} = \frac{\partial \Pi}{\partial \tilde{\lambda}^T} = A \int_{x_2}^{x_1} \{ N,_x(x)\tilde{u} - N(x)\tilde{\zeta} \} \, dx \qquad (28)$$

From Eqs. (26)–(28), the element stiffness matrices can be formulated. The stress–strain stiffness formulation, based on the first variational term of the foregoing equation, is standard and need not be discussed. To use more realistic and more complex damage constitutive relations such as the microplane model, this must be done incrementally.

Because the number of nodes is greater than the number of elements, the programming gets simpler by considering all λ_{ij} to be the nodal properties rather than the element properties. In one-dimensional analysis, this is done by using a linear function to approximate the Lagrange multiplier field λ in each finite element

$$\lambda = N(x)\tilde{\lambda} \quad \text{where} \quad \tilde{\lambda}^T = [\lambda_1, \lambda_2] \qquad (29)$$

Equations (26)–(28) now become

$$f_{int}^u = \frac{\partial \Pi}{\partial \tilde{u}^T}$$
$$= A \left\{ \int_{x_2}^{x_1} N^T,_x(x) \sigma_x \, dx - \int_{x_2}^{x_1} N^T,_x(x)N(x)\tilde{\lambda} \, dx - \int_{x_2}^{x_1} N^T(x)f(x) \, dx \right\} \qquad (30)$$

$$f_{int}^{\zeta} = \frac{\partial \Pi}{\partial \tilde{\zeta}^T} = A \left\{ \int_{x_2}^{x_1} N^T,_x(x) s_x \, dx + \int_{x_2}^{x_1} N^T(x)N(x)\tilde{\lambda} \, dx \right\} \qquad (31)$$

$$f_{int}^{\lambda} = \frac{\partial \Pi}{\partial \tilde{\lambda}^T} = A \int_{x_2}^{x_1} N^T(x) \{ N,_x(x)\tilde{u} - N(x)\tilde{\zeta} \} \, dx \qquad (32)$$

7.2 2D Formulation.
Consider now a 2D linear quadrilateral element of constant thickness b. If we set λ to be an element property, then, aside from nodes 1, 2, 3, and 4 serving as vertex nodes, node 5 is needed to store λ. This node is imagined to reside at the center of the element, denoted by coordinates (x, y). If we consider λ as the DOF at node 5, there are six DOF at each of nodes 1–4, forming the vector (or column matrix)

$$\bar{u}_j = [u_j, v_j, \zeta_j^{u,x}, \zeta_j^{u,y}, \zeta_j^{v,x}, \zeta_j^{v,y}]^T \quad \text{where} \quad j = 1, 2, 3, 4 \qquad (33)$$

and four DOF for node 5, forming the vector

$$\bar{\lambda}_5 = [\lambda^{u,x}, \lambda^{u,y}, \lambda^{v,x}, \lambda^{v,y}]^T \qquad (34)$$

Here $\zeta^{u,x}, \zeta^{u,y}, \zeta^{v,x}$, and $\zeta^{v,y}$ (dimensionless) are the approximations of displacement gradients u_x, u_y, v_x, and v_y, respectively, weakly imposed by the corresponding Lagrange multiplier $\lambda^{u,x}, \lambda^{u,y}, \lambda^{v,x}$, and $\lambda^{v,y}$ (dimension Pa); see Fig. 3 (the notation u is reserved for $(u, v)^T$). Therefore, we have 28 DOF per element.

For u and v, the linear field of the generalized displacements within the quadrilateral is defined by the shape (or interpolation) functions $N(x, y)$ for displacements u and v, and $N_\zeta(x, y)$ for the ζ field. In matrix form,

$$u(x, y) = N(x, y) \cdot \tilde{u} \quad \text{where} \qquad (35)$$

$$\tilde{u}^T = [u_1, v_1, u_2, v_2, u_3, v_3, u_4, v_4] \qquad (36)$$

$$\zeta(x, y) = N_\zeta(x, y) \cdot \tilde{\zeta} \quad \text{where} \qquad (37)$$

$$\tilde{\zeta}^T = [\zeta_1^{u,x}, \zeta_1^{u,y}, \zeta_1^{v,x}, \zeta_1^{v,y}, \zeta_2^{u,x}, \zeta_2^{u,y}, \zeta_2^{v,x}, \zeta_2^{v,y}, \zeta_3^{u,x}, \zeta_3^{u,y}, \zeta_3^{v,x}, \zeta_3^{v,y}, \zeta_4^{u,x}, \zeta_4^{u,y}, \zeta_4^{v,x}, \zeta_4^{v,y}] \qquad (38)$$

We can now minimize the total potential energy Π by setting the partial derivative of the total potential energy with respect to the degrees-of-freedom to be zero

$$f_{int}^u = \frac{\partial \Pi}{\partial \tilde{u}^T} = b \left\{ \int_A B_1^T \sigma \, dA - \int_A B_3^T \lambda \, dA - \int_A N^T(x, y)f(x, y) \, dA \right\} \qquad (39)$$

$$f_{int}^{\zeta} = \frac{\partial \Pi}{\partial \tilde{\zeta}^T} = b \left\{ \int_A B_2^T s \, dx + \int_A N_\zeta^T(x, y)\lambda \, dA \right\} \qquad (40)$$

$$f_{int}^{\lambda} = \frac{\partial \Pi}{\partial \tilde{\lambda}^T} = b \int_A \{ B_3 \tilde{u} - N_\zeta(x, y)\tilde{\zeta} \} \, dA \qquad (41)$$

where $B_1 = L_1 N(x, y)$, $B_2 = L_2 N_\zeta(x, y)$, and $B_3 = L_3 N(x, y)$. The definition of the matrices L_1, L_2, and L_3 are given as follows:

$$L_1^T = \begin{bmatrix} \partial/\partial & x & 0\partial/\partial y \\ 0 & \partial/\partial y & \partial/\partial x \end{bmatrix} \qquad (42)$$

$$L_2^T = \begin{bmatrix} \partial/\partial x & \partial/\partial y & 0 & 0 & 0 & 0 & 0 & 0 \\ 0 & 0 & \partial/\partial x & \partial/\partial y & 0 & 0 & 0 & 0 \\ 0 & 0 & 0 & 0 & \partial/\partial x & \partial/\partial y & 0 & 0 \\ 0 & 0 & 0 & 0 & 0 & 0 & \partial/\partial x & \partial/\partial y \end{bmatrix} \qquad (43)$$

$$L_3^T = \begin{bmatrix} \partial/\partial x & \partial/\partial y & 0 & 0 \\ 0 & 0 & \partial/\partial x & \partial/\partial y \end{bmatrix} \qquad (44)$$

If we consider λ to be a nodal property, then for each node, there will be four nodal values of λ corresponding to each component of the ζ tensor

$$\lambda = N_\lambda^T(x, y) \cdot \tilde{\lambda} \quad \text{where} \qquad (45)$$

$$\tilde{\lambda}^T = [\lambda_1^{u,x}, \lambda_1^{u,y}, \lambda_1^{v,x}, \lambda_1^{v,y}, \lambda_2^{u,x}, \lambda_2^{u,y}, \lambda_2^{v,x}, \lambda_2^{v,y}, \lambda_3^{u,x}, \lambda_3^{u,y}, \lambda_3^{v,x}, \lambda_3^{v,y}, \lambda_4^{u,x}, \lambda_4^{u,y}, \lambda_4^{v,x}, \lambda_4^{v,y}] \qquad (46)$$
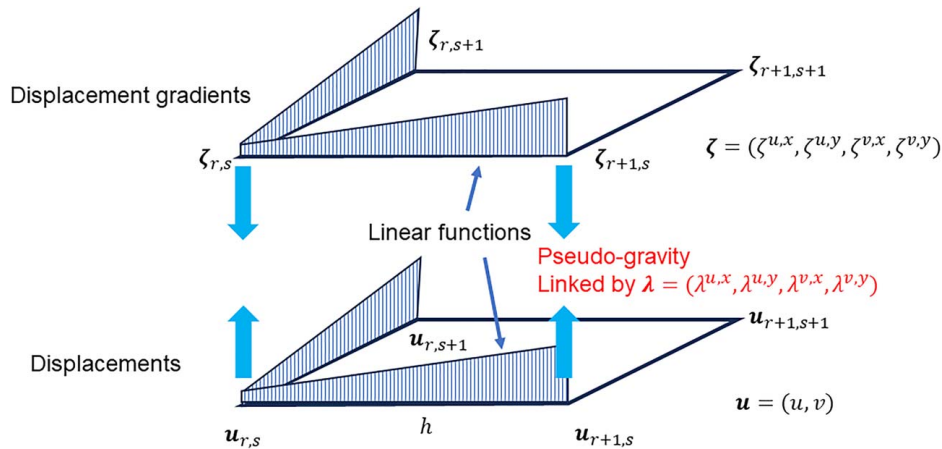
Fig. 3 Physical motivation: The actual displacement gradient tensor is contrained to the approximate displacement gradient tensor ζ through the use of the Lagrange multiplier tensor λ, which is an unknown constant moment density acting as "pseudo-gravity" working on the difference between the actual and the approximate gradient tensor. Linear shape functions are used for both the displacement field u and the approximate displacement gradient field ζ. Here, both ζ and λ are expressed in matrix form, and r,s are the generalized nodal numbers in the x and y directions.

Equations (38)–(40) can now be rewritten as

$$\boldsymbol{f}_{int}^{u} = \frac{\partial \Pi}{\partial \tilde{\boldsymbol{u}}^{T}}$$
$$= b \left\{ \int_{A} \boldsymbol{B}_{1}^{T} \boldsymbol{\sigma} \, \mathrm{d}A - \int_{A} \boldsymbol{B}_{3}^{T} N_{\lambda}(x,y) \tilde{\lambda} \, \mathrm{d}A - \int_{A} N^{T}(x,y) \boldsymbol{f}(x,y) \, \mathrm{d}A \right\}$$
(47)

$$\boldsymbol{f}_{int}^{\zeta} = \frac{\partial \Pi}{\partial \tilde{\boldsymbol{\zeta}}^{T}} = b \left\{ \int_{A} \boldsymbol{B}_{2}^{T} \boldsymbol{s} \, \mathrm{d}x + \int_{A} N_{\zeta}^{T}(x,y) N_{\lambda}(x,y) \tilde{\lambda} \, \mathrm{d}A \right\}$$
(48)

$$\boldsymbol{f}_{int}^{\lambda} = \frac{\partial \Pi}{\partial \tilde{\lambda}^{T}} = b \int_{A} N_{\lambda}^{T}(x,y) \left\{ \boldsymbol{B}_{3} \tilde{\boldsymbol{u}} - N_{\zeta}(x,y) \tilde{\boldsymbol{\zeta}} \right\} \mathrm{d}A$$
(49)

In ABAQUS, one must use the user element (UEL) feature. For computations, the tensors and vectors are represented by matrices. However, keep in mind that $u_{i,j}$, and also λ_{ij}, are generally nonsymmetric and must be represented by 4×1 column matrices. The integral can be evaluated for each finite element, which results into the expressions for stiffness matrices of the finite element.

Remark 2. Since the spress, s_{ijk}, does not work on strain ε_{ij} and stress σ_{ij} does not work on sprain ξ_{ijk}, we can look at our finite element system as two separate systems of four-node C_0 elements:

- One system with two nodal variables u and v, which has elements of C_0 continuity.
- The other system with four nodal variables $\zeta^{u,x}$, $\zeta^{u,y}$, $\zeta^{v,x}$ and $\zeta^{v,y}$ each node (Fig. 3). Taken alone, the elements of this system have also C_0 continuity, but since here the variables are the approximate displacement gradients, the C_1 continuity (across the element boundaries) is ensured (in the approximate sense) for the finite element system as a whole. The approximate displacement gradients are transmitted to the adjacent element.
- The two systems interact only through the Lagrange multiplier λ, as described by the term $\lambda(\nabla \boldsymbol{u} - \boldsymbol{\zeta})$ in Eq. (11), which may be regarded as the external work $W_{\zeta} = \lambda \Delta_{\zeta}$. It may be perceived as the pseudo-gravity λ (a constant generalized moment per unit volume) working on the gradient difference $\Delta_{\zeta} = \nabla \boldsymbol{u} - \boldsymbol{\zeta}$. If $\Delta_{\zeta} \to 0$, then the external work $W_{\zeta} \to 0$. ∎
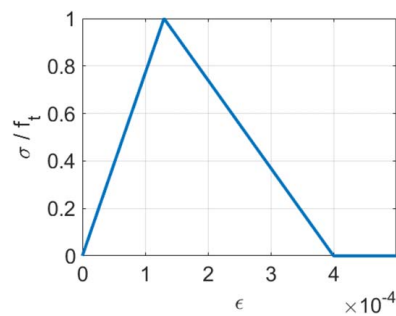

Fig. 4 Bilinear stress versus strain response of the material of the 1D bar under uniaxial tension

8 Examples of Numerical Simulations of Fracture

This paper is focused on the computational aspects of the sprain theory, while the physical aspects with the comparisons to the results of various types of fracture test are relegated to a subsequent article. Computer simulation results for the uniaxial tension of a 1D bar and the three-point bend fracture test are presented.

8.1 1D Bar Under Uniaxial Tension. Consider a one-dimensional bar of length $L = 100$ mm using a material
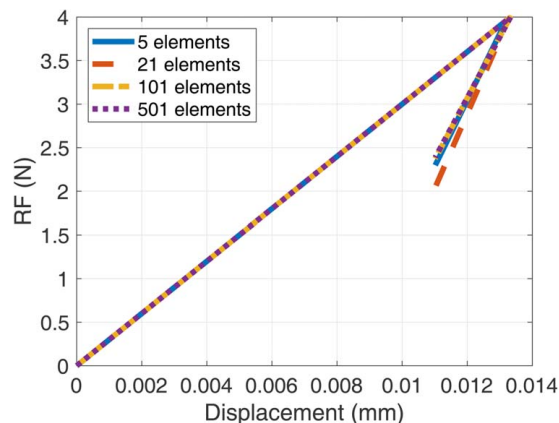

Fig. 5 Reaction force versus displacement at the boundary of the bar when it is discretized into 5, 21, 101, and 501 elements
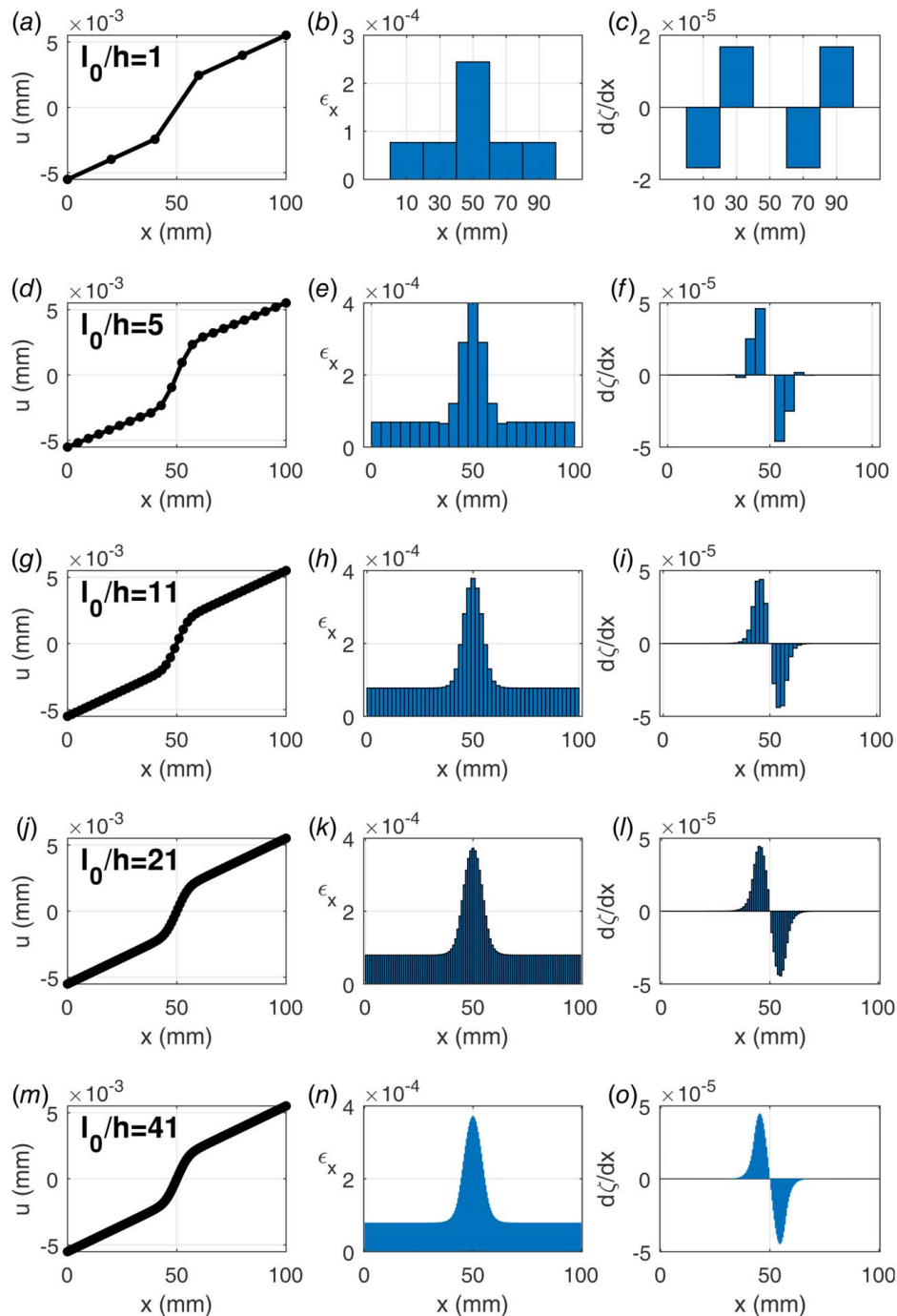
Fig. 6 From left to right: Displacement profile *u*, strain profile *ε*, and approximated sprain profile d*ζ*/dx of the 1D bar under uniaxial tension that is discretized into (from top to bottom) 5, 21, 51, 101, and 201 elements

following a simple bilinear elastic softening stress–strain relation with a Young's modulus of $E = 30$ GPa and a tensile strength of $f_t = 4$ MPa (Fig. 4). The corresponding elastic strain at the tensile strength limit is $\varepsilon_0 = f_t/E$ and the strain after complete softening, ε_c, is chosen such that $\varepsilon_c/\varepsilon_0 = 3$. The characteristic length l_0 is 20 mm. In the original CBM, the crack bandwidth is equal to the characteristic length l_0 and the strain, $\varepsilon = u'$, is uniform across the band. Here, l_0 is subdivided into several uniform-strain elements and the width of the crack band is roughly equal to the characteristic length. Specifically, the bar is discretized into 5, 21, 51, 101, 201, and 501 elements, and the characteristic length l_0 is thus divided into 1, 5, 11, 21, 41, and 101 elements, respectively.

The middle element of the bar will have a slightly reduced tensile strength of 0.99 f_t, in order to induce strain localization at the middle of the bar. The spress-sprain relation used is based on the Eq. (13) with the threshold $C = 0$ and the sprain stiffness $\kappa = 127.5$ GPa.

This is a static problem, and an implicit static algorithm is used. To capture the snapback behavior, a simple algorithm inspired by the crack mouth opening displacement control is used. First, since it is known that the middle (weakest) element is always stretched after each increment, a pair of displacement increments equal in magnitude but opposite in direction is prescribed at the two nodes of the middle element. After that, the nodal displacements at the
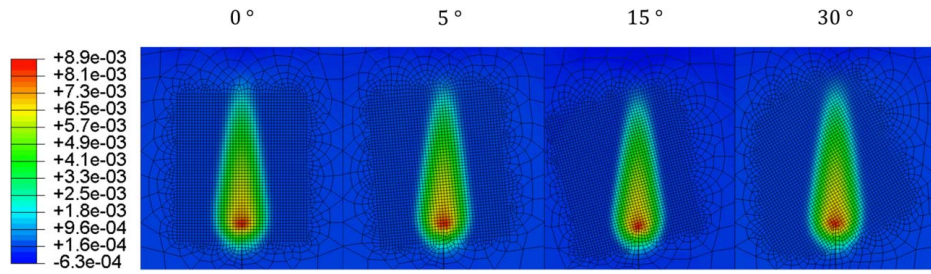
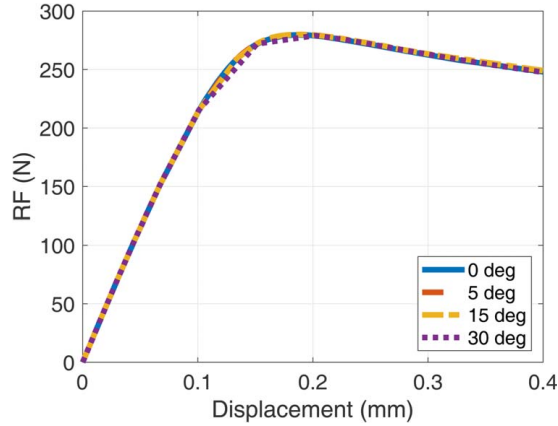**Fig. 7 Three-point bend simulations with different mesh inclinations using the sICBM and M7**

Fig. 8 Reaction force versus displacement of the loading point at the top of the specimen with different mesh inclinations

two boundaries (along with the rest of the DOF) will be obtained using standard Newton–Raphson algorithm with the conditions that the reaction forces at the two nodes of the middle element equal to zero.

The displacement field, strain field, and the approximate sprain field which is the gradient of ζ of the bar are discretized into different numbers of elements, as shown in Fig. 6. The original CBM is used when l_0 is equal to the width of the element (Figs. 6(a), 6(b), and 6(c)). As the bar is discretized into more elements, through the use of the localization resisting sprain energy, the damage gets spread over the characteristic length l_0 with a smooth bell-type distribution using a proper chosen sprain stiffness κ. Figure 5 shows the force versus displacement curves as the bar is discretized into different numbers of elements. Because the strain field is uniform during elastic loading, the elastic response is the same with or without using the sprain energy; therefore, setting the threshold C to be zero is justified. Note that the localization resistance should decrease as the damage increases and vanish when the material is totaly broken, since there will be residual stresses in the bar if a constant sprain stiffness κ is used for post-peak damage [4]. The simulation using a constant sprain

stiffness κ is thus terminated near post-peak damage before the residual stresses become large enough to affect the force versus displacement curve.

The strain field (Figs. 6(b), 6(e), 6(h), 6(k), and 6(n)) and the approximate sprain field (Figs. 6(c), 6(f), 6(i), 6(l), and 6(o)) smooth and converge as the number of finite elements increases. The convergence can also be shown by the plot of the L_2 norm of the error of the reaction force of the system, i.e., $L_2 = \|F - F_{asympt}\|_2$. Here F_{asympt} would be the exact loading force for the given load-point displacement if the exact value were known a priori. Since it is not known, we determine the value F_{asympt} so that the computed value in the log-log plot of Fig. 10(a) falls into a straight line, and a straight line in the log-log scale represents a power law. A linear regression fitting line shows that the rate of convergence is at least quadratic.

8.2 2D Three-Point Bend Test Simulation. The specimen geometry for the three-point bend test simulation is similar to that used in Ref. [4] but the material model is the M7 microplane model for concrete. Note that different parameter combinations for M7 microplane model correspond to different material properties; it is an important process for objectively describing a quasi-brittle material, which is also detailed in Ref. [43]. Here the elastic (Young's) modulus is $E = 38.3$ GPa, the Poisson ratio is $\nu = 0.18$. The calibrated M7 (implicit) parameters were $k_1 = 0.00015$, $k_2 = 110$, $k_3 = 30$, $k_4 = 100$. The threshold $C = 0$ and the sprain stiffness $\kappa = 1.9$ GPa. The span-to-depth ratio is $L/D = 3.8$ and the notch depth is $a/D = 0.197$.

Figure 7 shows the simulation results when a fine square mesh in a zone surrounding the growing crack is deliberately inclined from the notch line at various angles equal to 0 deg, 5 deg, 15 deg, and 30 deg. The mesh size in the near-tip zone is $l_0/20$. Each element is a four-node finite element with linear shape functions for u, ζ and the Lagrange multiplier λ, as already described. Figure 7 compares the widths and shapes of the fracture process zone and demonstrates that the contours of constant transverse strains ε_{xx} of different magnitudes are virtually identical. Similarly, the difference between the values of the center-span equilibrium loading force as a function of the vertical load-point displacement for different mesh inclinations is negligible (Fig. 8).
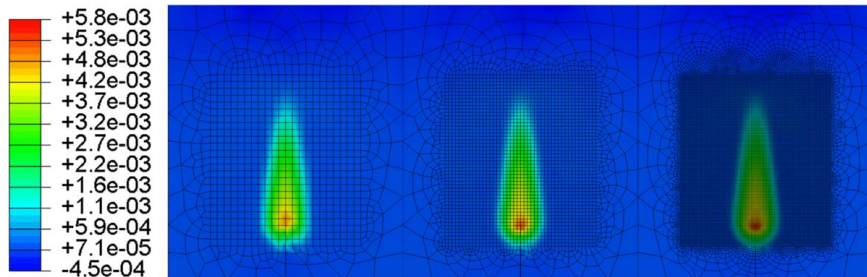

Fig. 9 Convergence check of the sICBM, from left to right the mesh gradually becomes denser with the same geometry
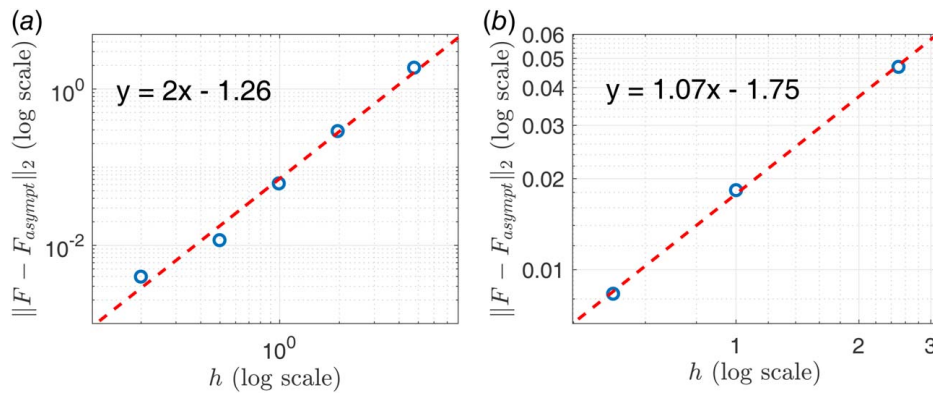
Fig. 10 L_2 norm of the error for the reaction force of the (*a*) 1D bar under unaxial tension being discretized into 5, 21, 51, 101, 201, and 501 elements, and (*b*) 2D three-point bend fracture specimens using the square element sizes near crack tip of 5 mm, 2.5 mm, and 1 mm. An asymptotic loading force F_{asympt} is used in place of the exact loading force here. F_{asympt} is determined so that the computed value in the log-log plot falls into a straight line, representing a power law.

Figure 9 shows the effect of changing mesh size near the crack tip, considering the same identical three-point bend fracture specimens and simulation setup. The square element sizes are chosen as 5 mm, 2.5 mm, and 1 mm, respectively. The results are not only stable but also almost independent of the element size, overcoming the mesh bias. Figure 9 is a practical demonstration of convergence of the present method with linear shape functions and Lagrange multipliers. Figure 10(*b*) shows the plot of the L_2 norm of the error of the reaction force of the system. Similar to the 1D simulation, here F_{asympt} is determined as the force value for which the L_2 norm of the error of the reaction force falls into the straight line in the log-log plot, representing a power law. An approximate power law must be expected because of the nearly perfect similarity of the three meshes of different refinements.

9 Conclusions

(1) Computer implementation of the previously proposed concept of limiting damage localization by applying sprain forces on adjacent nodes of a finite element [4] runs into formidable obstacles. It is tedious to program and extends the running time on commercial FE codes such as ABAQUS by almost two orders of magnitude.

(2) What helps to eliminate this problem is to consider both the displacement vector $\boldsymbol{u}$ with components u and v and the approximate gradient tensor $\boldsymbol{\zeta}$ with components $\zeta^{u,x}$, $\zeta^{u,y}$, $\zeta^{v,x}$, $\zeta^{v,y}$ as independent nodal variables.

(3) The approximate gradient components are constrained to the actual gradient components u_x, u_y, v_x, v_y by means of Lagrangian multipliers $\lambda^{u,x}$, $\lambda^{u,y}$, $\lambda^{v,x}$, $\lambda^{v,y}$ applied to the difference between the actual and approximate gradients. Zeroing of the derivatives of the Helmholtz free energy of the structure with respect to the Lagrange multipliers of all the nodes gives the optimum constraint yielding the best approximation of the actual displacement gradient tensor.

(4) The gradient tensor of the approximate gradient tensor represents the approximate curvature of the displacement vector. Their limitation by means of the spress-sprain relation based on the sprain energy prevents spurious damage localization at, and behind, the fracture front of finite width. In the generalized stiffness matrix, this is effected by the matrix components representing spress-based resistance to sprain.

(5) The Lagrange multipliers can be considered as element properties or the nodal properties. The former is more efficient by reducing the total number of DOF, while treating the Lagrange multipliers as nodal properties aid the programming in commercial FEA software such as ABAQUS.

(6) Thanks to adopting approximate displacement gradients as independent nodal variables and constraining them by Lagrangian multipliers, there is no need for localization control by sprain forces applied on the nodes of the adjacent elements.

(7) Physically, the Lagrange multipliers represent applied generalized moments per unit volume working on the gradient differences. It is important that their work is not part of the internal Helmholtz free energy stored in the material but is external, like the work of gravity forces.

(8) In two-dimensional fracture modeling, there are ten unknown degrees-of-freedom per node: two nodal displacement components, four approximate displacement gradients, and four Lagrange multipliers. The increased number of variables requires introducing into a user's element of ABAQUS a larger and more complex stiffness matrix.

(9) A severe test in computer simulations is the mesh bias and convergence when the material characteristic length is subdivided into more elements. FE simulations with ABAQUS show both tests to be verified. If the material characteristic length l_0 is subdivided into five elements or more, the directional bias of a square mesh is totally eliminated.

(10) In contrast to the CBM, the slCBM can simulate the variation of the crack band width due to loading and to crack growth. Importantly, the width of the crack band (or damage zone) remains nearly the same for different subdivisions. Mesh rotations by 5 deg, 15 deg, 30 deg make no discernible difference. Although the mesh orientation independence was demonstrated in the preceding study, it was at the cost of great programming difficulties as well as huge computational burden and enormous running time.

Acknowledgement

Conflict of Interest

There are no conflicts of interest.

Data Availability Statement

The program used to generate the computer results is posted on Z. P. Bažant's website.

References

[1] Clough, R. W., 1962, "The Stress Distribution of Norfork Dam," Institute of Engineering Research, Final Report to the Corps of Engineers.

[2] Clough, R. W., and Wilson, E. L., 1962, "Stress Analysis of a Gravity Dam by the Finite Element Method," Laboratório Nacional de Engenharia Civil.

[3] Clough, R. W., 1960, "The Finite Element Method in Plane Stress Analysis," Proceedings of 2nd ASCE Conference on Electronic Computation, Pittsburgh, PA, Sept. 8–9.

[4] Zhang, Y., and Bažant, Z. P., 2023, "Smooth Crack Band Model-A Computational Paragon Based on Unorthodox Continuum Homogenization," ASME J. Appl. Mech., 90(4), p. 041007.

[5] Bažant, Z. P., Nguyen, H. T., and Abdullah Dönmez, A., 2022, "Critical Comparison of Phase-Field, Peridynamics, and Crack Band Model M7 in Light of Gap Test and Classical Fracture Tests," ASME J. Appl. Mech., 89(6), p. 061008.

[6] Nguyen, H. T., Pathirage, M., Cusatis, G., and Bažant, Z. P., 2020, "Gap Test of Crack-Parallel Stress Effect on Quasibrittle Fracture and Its Consequences," ASME J. Appl. Mech., 87(7), p. 071012.

[7] Nguyen, H., Pathirage, M., Rezaei, M., Issa, M., Cusatis, G., and Bažant, Z. P., 2020, "New Perspective of Fracture Mechanics Inspired by Gap Test With Crack-Parallel Compression," Proc. Natl. Acad. Sci. U. S. A., 117(25), pp. 14015–14020.

[8] Bažant, Z. P., Le, J. -L., and Salviato, M., 2021, Quasibrittle Fracture Mechanics and Size Effect: A First Course, Oxford University Press, Oxford, UK.

[9] Bažant, Z. P., and Nguyen, H. T., 2023, "Proposal of M-Index for Rating Fracture and Damage Models by Their Ability to Represent a Set of Distinctive Experiments," J. Eng. Mech., 149(8), p. 04023047.

[10] Bažant, Z. P., and Oh, B. H., 1983, "Crack Band Theory for Fracture of Concrete," Matériaux et Constr., 16, pp. 155–177.

[11] Červenka, J., Bažant, Z. P., and Wierer, M., 2005, "Equivalent Localization Element for Crack Band Approach to Mesh-Sensitivity in Microplane Model," Int. J. Numer. Meth. Eng., 62(5), pp. 700–726.

[12] Nguyen, H. T., Caner, F. C., and Bažant, Z. P., 2021, "Conversion of Explicit Microplane Model With Boundaries to a Constitutive Subroutine for Implicit Finite Element Programs," Int. J. Numer. Meth. Eng., 122(6), pp. 1563–1577.

[13] Bažant, Z. P., and Jirásek, M., 2002, "Nonlocal Integral Formulations of Plasticity and Damage: Survey of Progress," J. Eng. Mech., 128(11), pp. 1119–1149.

[14] Cusatis, G., Bažant, Z. P., and Cedolin, L., 2003, "Confinement-Shear Lattice Model for Concrete Damage in Tension and Compression: I. Theory," J. Eng. Mech., 129(12), pp. 1439–1448.

[15] Cusatis, G., Pelessone, D., and Mencarelli, A., 2011, "Lattice Discrete Particle Model (LDPM) for Failure Behavior of Concrete. I: Theory," Cem. Concr. Compos., 33(9), pp. 881–890.

[16] Mindlin, R., and Tiersten, H. F., 1962, "Effects of Couple-Stresses in Linear Elasticity," Arch. Ration. Mech. Anal., 11(1), pp. 415–448.

[17] Toupin, R., 1962, "Elastic Materials With Couple-Stresses," Arch. Ration. Mech. Anal., 11(1), pp. 385–414.

[18] Eringen, A. C., 1965, Theory of Micropolar Elasticity, Springer, New York, NY.

[19] Bažant, Z. P., and Christensen, M., 1972, "Analogy Between Micropolar Continuum and Grid Frameworks Under Initial Stress," Int. J. Solids Struct., 8(3), pp. 327–346.

[20] Fleck, N., and Hutchinson, J., 1993, "A Phenomenological Theory for Strain Gradient Effects in Plasticity," J. Mech. Phys. Solids, 41(12), pp. 1825–1857.

[21] Cosserat, E., and Cosserat, F., 1909, Théorie Des Corps Déformables (Theory of Deformable Bodies), A. Hermann & Fils, Paris.

[22] Gao, H., Huang, Y., Nix, W., and Hutchinson, J., 1999, "Mechanism-Based Strain Gradient Plasticity–I. Theory," J. Mech. Phys. Solids, 47(6), pp. 1239–1263.

[23] Huang, Y., Gao, H., Nix, W., and Hutchinson, J., 2000, "Mechanism-Based Strain Gradient Plasticity–II. Analysis," J. Mech. Phys. Solids, 48(1), pp. 99–128.

[24] Caner, F. C., and Bažant, Z. P., 2013, "Microplane Model M7 for Plain Concrete. I: Formulation," J. Eng. Mech., 139(12), pp. 1714–1723.

[25] Caner, F. C., and Bažant, Z. P., 2013, "Microplane Model M7 for Plain Concrete. II: Calibration and Verification," J. Eng. Mech., 139(12), pp. 1724–1735.

[26] Li, C., Caner, F. C., Chau, V. T., and Bažant, Z. P., 2017, "Spherocylindrical Microplane Constitutive Model for Shale and Other Anisotropic Rocks," J. Mech. Phys. Solids, 103, pp. 155–178.

[27] Kirane, K., Salviato, M., and Bažant, Z. P., 2016, "Microplane-Triad Model for Elastic and Fracturing Behavior of Woven Composites," ASME J. Appl. Mech., 83(4), p. 041006.

[28] Nye, J. F., 1953, "Some Geometrical Relations in Dislocated Crystals," Acta Metall., 1(2), pp. 153–162.

[29] Voigt, W., 1889, "Ueber Die Beziehung Zwischen Den Beiden Elasticitätsconstanten Isotroper Körper," Annalen der physik, 274(12), pp. 573–587.

[30] Reuß, A., 1929, "Berechnung Der Fließgrenze Von Mischkristallen Auf Grund Der Plastizitätsbedingung Für Einkristalle.," ZAMM-J. Appl. Math. Mech./ Zeitschrift für Angewandte Mathematik und Mechanik, 9(1), pp. 49–58.

[31] Eshelby, J. D., 1957, "The Determination of the Elastic Field of an Ellipsoidal Inclusion, and Related Problems," Proc. R. Soc. London, A, 241(1226), pp. 376–396.

[32] Hashin, Z., and Shtrikman, S., 1963, "A Variational Approach to the Theory of the Elastic Behaviour of Multiphase Materials," J. Mech. Phys. Solids, 11(2), pp. 127–140.

[33] Hashin, Z., 1988, "The Differential Scheme and Its Application to Cracked Materials," J. Mech. Phys. Solids, 36(6), pp. 719–734.

[34] Hill, R., 1965, "A Self-Consistent Mechanics of Composite Materials," J. Mech. Phys. Solids, 13(4), pp. 213–222.

[35] Mori, T., and Tanaka, K., 1973, "Average Stress in Matrix and Average Elastic Energy of Materials With Misfitting Inclusions," Acta Metall., 21(5), pp. 571–574.

[36] Hutchinson, J., and Fleck, N., 1997, "Strain Gradient Plasticity," Adv. Appl. Mech., 33, pp. 295–361.

[37] Hutchinson, J. W., 1968, "Plastic Stress and Strain Fields at a Crack Tip," J. Mech. Phys. Solids, 16(5), pp. 337–342.

[38] Hutchinson, J. W., and Paris, P. C., 1979, "Stability Analysis of J-Controlled Crack Growth," Elastic-Plastic Fracture, J. D. Landes, J. A. Begley, and G. A. Clarke, eds., ASTM International, Philadelphia, PA.

[39] Rektorys, K., 2013, Survey of Applicable Mathematics, Vol. 280, Springer, Netherlands.

[40] Zienkiewicz, O. C., Taylor, R. L., and Zhu, J. Z., 2005, The Finite Element Method: Its Basis and Fundamentals, Elsevier, Netherlands.

[41] Brezzi, F., and Fortin, M., 2011, Mixed and Hybrid Finite Element Methods, Springer New York, NY.

[42] Areias, P., and Matouš, K., 2008, "Stabilized Four-Node Tetrahedron With Nonlocal Pressure for Modeling Hyperelastic Materials," Int. J. Numer. Meth. Eng., 76(8), pp. 1185–1201.

[43] Xu, H., Dönmez, A. A., Nguyen, H. T., and Bažant, Z. P., 2023, "What We Can and Cannot Learn From a Single Shear Test of a Very Large Rc Beam," J. Struct. Eng., 149(9), p. 04023113.